Journal of Nanobiotechnology

RESEARCH

Open Access

An anti-CD19-exosome delivery system navigates the blood–brain barrier for targeting of central nervous system lymphoma

Meifang Zhao[1], Qi Li[1], Yali Chai[2], Rong Rong[3], Lexin He[4], Yuchen Zhang[1], Hongxia Cui[1], Hao Xu[1], Xinyun Zhang[1], Zhiming Wang[1], Shushu Yuan[1], Menglu Chen[1], Chuan He[1], Han Zhang[1], Linlin Qin[2], Ruijing Hu[2], Xinyuan Zhang[1], Wenzhuo Zhuang[2*] and Bingzong Li[1*]

Abstract

Background High-dose methotrexate (HD-MTX) serves as the cornerstone of central nervous system lymphoma (CNSL) treatment, but its efficacy is limited due to low blood–brain barrier (BBB) penetration and adverse effects. This study is focused on an exosome-based drug delivery approach aimed at enhancing BBB permeability, thereby reducing the required dosage of methotrexate (MTX) while ensuring specific targeting of CNSL.

Methods Human adipose-derived mesenchymal stem cells (hAMSCs) were modified with a lentiviral vector encoding anti-CD19, incorporated into exosomes characterized by colloidal gold immunoelectron microscopy and Nano flow cytometry. MTX loaded into anti-CD19-Exos via co-incubation, assessed for loading and encapsulation efficiencies using HPLC. In vitro BBB model constructed using hCMEC/D3 and astrocytes to investigate BBB permeability. In vivo efficacy of anti-CD19-Exo-MTX evaluated in intracranial CNSL models using MRI. Biodistribution tracked with DiR-labeled exosomes, drug concentration in CSF measured by HPLC. LC-MS/MS identified and characterized exosomal proteins analyzed using GO Analysis. Neuroprotective effects of exosomal proteins assessed with TUNEL and Nissl staining on hippocampal neurons in CNSL models. Liver and kidney pathology, blood biochemical markers, and complete blood count evaluated exosomal protein effects on organ protection and MTX-induced myelosuppression.

Results We generated anti-CD19-Exo derived from hAMSCs. These adapted exosomes effectively encapsulated MTX, enhancing drug accessibility within lymphoma cells and sustained intracellular accumulation over an extended period. Notably, anti-CD19-Exo-MTX interacted with cerebrovascular endothelial cells and astrocytes of the BBB, leading to endocytosis and facilitating the transportation of MTX across the barrier. Anti-CD19-Exo-MTX outperformed free MTX in vitro, exhibiting a more potent lymphoma-suppressive effect ($P < 0.05$). In intracranial orthotopic CNSL models, anti-CD19-Exo-MTX exhibited a significantly reduced disease burden compared to both the MTX and Exo-MTX groups, along with prolonged overall survival ($P < 0.05$). CSF drug concentration analysis demonstrated enhanced stability and longer-lasting drug levels for anti-CD19-Exo-MTX. Anti-CD19-Exo-MTX exhibited precise CNSL targeting with no organ toxicity. Notably, our study highlighted the functional potential of reversal effect of hAMSCs-exosomes on MTX-induced neurotoxicity, hepatic and renal impairment, and myelosuppression.

Conclusions We present anti-CD19-Exo-MTX as a promising exosome-based drug delivery platform that enhances BBB permeability and offers specific targeting for effective CNSL treatment with reduced adverse effects.

*Correspondence:
Wenzhuo Zhuang
zhuangwenzhuo@suda.edu.cn
Bingzong Li
lbzwz0907@hotmail.com
Full list of author information is available at the end of the article

Keywords Exosome, Drug delivery system, Targeted therapy, Central nervous system lymphoma, Blood–brain barrier, Methotrexate

Graphical Abstract

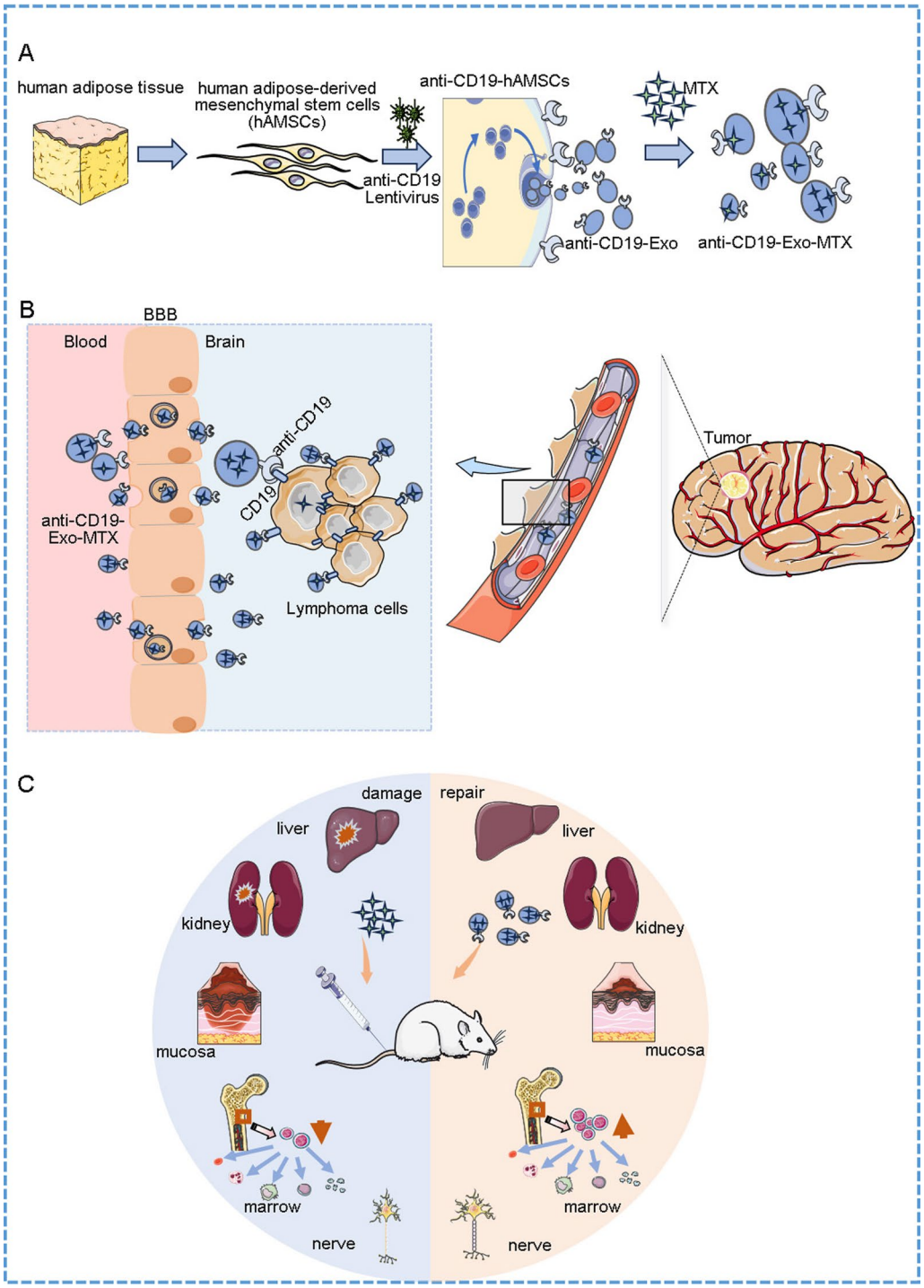

Introduction

Central nervous system lymphoma (CNSL) is a rare extra-nodal lymphomatous malignancy that primarily impacts the brain, spinal cord, leptomeninges, or vitreoretinal space [1]. While multiple treatments have shown efficacy against B-cell lymphoma, the clinical challenge is delivering chemotherapy agents to intracranial tumors due to the presence of the blood–brain barrier (BBB) [2]. Over the past few decades, the prognosis of CNSL has significantly improved, primarily attributed to the introduction and widespread utilization of high-dose methotrexate (MTX) chemotherapy, recognized as the cornerstone of first-line polychemotherapy treatment [1]. MTX is an inhibitor of dihydrofolate reductase (DHFR), which prevents the reduction of dihydrofolate to tetrahydrofolate by competitively binding to DHFR. This inhibition leads to a blockade in DNA synthesis, ultimately resulting in cell death [3]. When administered intravenously at high doses, MTX can cross the BBB, causing significant side effects such as neuronal damage, myelosuppression, hepatic injury and renal dysfunction [4]. Investigating a safe and effective system for delivering drugs directly into the brain presents a crucial opportunity to enhance the clinical remission rate and long-term therapeutic efficacy of CNSL.

In recent decades, significant progress has been made in the development of nanocarriers for drug delivery systems (DDS). A wide range of DDS have been explored for tumor treatment, including nanoscale formulations such as liposomes, polymeric nanoparticles, or metallic nanocarriers, although these nanoparticles often suffer from high immunogenicity and limited ability to cross the BBB [5]. The byproducts of polymeric nanoparticles may be toxic and difficult to eliminate, and the surface charge of liposomes can affect their stability in the bloodstream [6, 7]. Exosomes have garnered attention as "innate nanoparticles" for drug delivery [8]. Exosomes have been identified as important mediators of intercellular communication via transferring encapsulated cargoes, such as bioactive lipids, noncoding RNAs, mRNAs, and proteins [9, 10]. Exosomes employed as drug delivery vehicles offer numerous advantages over existing synthetic systems [11]. Firstly, the phospholipid bilayers of exosomes enable them to interact with cellular membranes and improve the cellular internalization of the encapsulated drug, potentially circumventing the endosome-lysosome pathway that synthetic materials typically undergo [12, 13]. Secondly, as exosomes can originate from autologous tissues or blood-born immunocytes, they may have an immune privileged status and decrease drug clearance compared to artificial delivery vehicles [14]. Of particular concern is that exosomes can traverse the BBB and the blood–cerebrospinal fluid barrier increasing the concentration of loaded drugs in the cerebrospinal fluid (CSF) [15, 16]. The distinctive characteristics of exosomes render them an appealing choice as a drug delivery system for treating CNS diseases.

Human adipose-derived mesenchymal stem cells (hAMSCs) can differentiate into pluripotent cells and secrete exosomes that inherit their low immunogenic profile, immune regulation, proliferation, and migration abilities [17]. Indeed, AMSCs are readily obtainable and can be easily expanded in vitro. Given the characteristics of hAMSCs, utilizing their exosomes as drug carriers presents an additional potential strategy for cancer therapy [18].

However, the practical applications of exosomes may be limited due to insufficient targeting ability or low efficacy in some cases [19]. Exosome targeting for drug delivery is critical to enhance drug accumulation at the target site and reduce off-target effects [20]. Various approaches have been applied to engineer cell-derived exosomes for higher selectivity and effectiveness, such as selecting specific donors or utilizing bioengineering techniques [19]. Surface modifications can enhance the targeting capability of exosomes [21, 22]. The prevailing approach lately involves the "cell engineering" technique, where donor cells are engineered to generate ligand-conjugated or drug-loaded exosomes [23–25]. CD19 is a cell surface marker primarily expressed on B cells, including all stages of B cell development, except for plasma cells. It plays a key role in B cell activation, differentiation, and immune response. The CD19 antigen is highly expressed and specifically localized on the surface of malignant mature B lymphocytes, which makes it an ideal target for therapeutic interventions, including exosome-based delivery systems. The use of anti-CD19 for targeted therapy, which has proven effective in treating various B-cell malignancies such as B-cell non-Hodgkin lymphoma, enhances the precision of therapeutic interventions while minimizing associated toxicity [26].

In this study, we explored the feasibility of delivering the chemotherapeutic drug MTX to overcome the BBB to tumor tissue using engineered exosomes. Anti-CD19 was modified on the exosomes extracted from hAMSCs, while MTX was encapsulated within these extracted exosomes to prepare the anti-CD19-Exo-MTX drug delivery system. The high antitumor activity of the anti-CD19-Exo-MTX was then validated both in vitro and in vivo in CNSL, while also reducing adverse effects.

Methods and materials

Cell culture and preparation

hAMSCs were extracted from human adipose tissue. SU-DHL-8, HEK-293T, hCMEC/D3, HA, HT22 and HK-2 cell lines were purchased from the American Type

Culture Collection. The cell lines were authenticated through short tandem repeat profiling conducted by the cell line characterization core (Genetic Testing Biotechnology Corporation, China).

Preparation of anti-CD19 modified hAMSCs

For the genetic modification of anti-CD19 to hAMSCs, anti-CD19 lentivirus encoding a CAR comprising an FMC63-derived CD19-specific scFv fused to a modified CD8α-hinge spacer, a CD28 transmembrane domain, and a CD3ζ signaling domain, with GFP labeling (Additional file 1 Figure S1A) were added to the cells to allow precise enumeration of transduced hAMSCs by flow cytometry. Then polybrene with a final concentration of 8 μg/mL was added. After 48 hours of culture, non-modified hAMSCs served as control cells to establish the threshold for the hAMSC population using a Sony automated flow cytometer with FITC-GFP emission filters (Additional file 1 Figure S1E). The FITC-GFP-labeled hAMSCs were then sorted and cultured.

Isolation and characterization of exosomes

Exosomes were isolated from the hAMSCs culture medium by a differential centrifugation method. In brief, the collected cell-conditioned medium was centrifuged at 300×*g* for 5 min, 2000×*g* for 15 min, and 10,000×*g* for 30 min. After filtration with a 0.22 μm filter, the filtrate was centrifuged at 100,000×*g* for 2 h at 4 °C. The pellet was resuspended in PBS and subsequently centrifugated at 100,000×*g* for another 2 h. The pellets were resuspended with PBS and analyzed using a BCA Protein Assay kit (Beyotime Biotechnology) to quantify the protein content of exosomes for subsequent experiments.

Western blot

The exosomes were lysed in RIPA lysis buffer (Yeasen), and equal amounts of protein were separated by SDS-PAGE gels and transferred to PVDF membranes (Merck Millipore, MA, USA). The blots were blocked with 5% BSA Tween-20 (0.1%) PBS buffer (T-PBS, pH 7.4) for 1 h at room temperature. The membranes were incubated with primary antibodies at 4 °C overnight, followed by incubation with HRP-linked secondary antibodies at 37 °C for 1 h. Antibodies were: anti-CD63 (proteintech, 25682); anti-CD81 (proteintech, 66866); anti-TSG1013 (proteintech, 67381); anti-Albumin (proteintech, 16475).

Dynamic light scattering (DLS)

A 10 μL aliquot from the resuspended exosome sample was diluted in 990 μL of PBS and mixed well. The size distribution and Zeta potential of exosome were analyzed using the Zetasizer Nano ZS90 (Malvern, UK). Three determinations per sample were taken at room temperature, the resulting data were analyzed with the Malvern software (Zetasizer Ver. 7.11).

Transmission electron microscopy (TEM)

10uL exosome suspension was dropped onto Formvar-carbon-coated EM grids (Alliance Biosystems, Japan) and stained with 2% phosphotungstic acid. The resulting samples were examined with a Tecnai G2 spirit BioTwin electron microscope (FEI, USA).

Colloidal gold immunoelectron microscopy

Purified exosomes were placed on Formvar-carbon-coated EM grids and fixed with paraformaldehyde, blocked, followed by incubation with a 10-nm protein gold conjugate (BBI Solutions, Cardiff, UK) for 20 min to label the anti-CD19. Each staining step was followed by three TBST washes and then staining with 1% glutaraldehyde. Then, grids were air-dried and visualized using a transmission electron microscope. Anti-CD19 on the surface of anti-CD19-Exo exosomes was specifically labeled with gold nanoparticles, while no staining was observed on unmodified exosomes.

Flow cytometry

At least 10,000 events were acquired using different emission filters, using a FACSVerse Flow Cytometer (BD, USA). The gating strategy used to identify viable cells and

(See figure on next page.)

Fig. 1 Characterization of human AMSCs and the preparation of hAMSCs-derived anti-CD19-Exo. **A** Cellular morphology of hAMSCs in culture (× 200 magnification). **B** Flow cytometry analysis of the surface markers in hAMSCs. **C, D** Oil Red O staining in hAMSCs cultured in adipogenesis differentiation medium for 14 days (**C**) and the expression levels of LPL and PPAR were detected by quantitative PCR (**D**) (n = 3). Scale bar, 50μm. **E, F** BCIP/NBT Alkaline Phosphatese staining in ADSCs cultured in osteogenesis differentiation medium for 14 days (**E**) and the expression levels of ALP, OCN and Runx2 were detected by quantitative PCR (**F**) (n = 3) Scale bar, 100μm. **G** Flow sorting of anti-CD19 positive hAMSCs. **H** Zeta potential and size distribution of hAMSCs-derived exosomes and anti-CD19-Exo determined by dynamic light scattering (DLS). **I** CD63, CD81, TSG101and Albumin of exosomal markers were detected in hAMSCs-derived exosomes and anti-CD19-Exo by Western blot assay. **J, K** Representative image of anti-CD19-Exo via transmission electron microscopy (TEM) (Scale bar, 100nm) (**J**) and immunogold microscopy (Red arrows indicate colloidal gold particles, scale bar, 50 nm) (**K**). **L** The expression of anti-19, CD81 and CD63 on the surface of anti-CD19-Exo membrane were detected by nano-flow cytometry. Data are shown as mean ± SEM, and the experiment was performed three times and a representative example is shown. **D** and **F** were analyzed by unpaired two-tailed Student's *t*-test. **P* < 0.05, ***P* < 0.01, ****P* < 0.001, *****P* < 0.0001

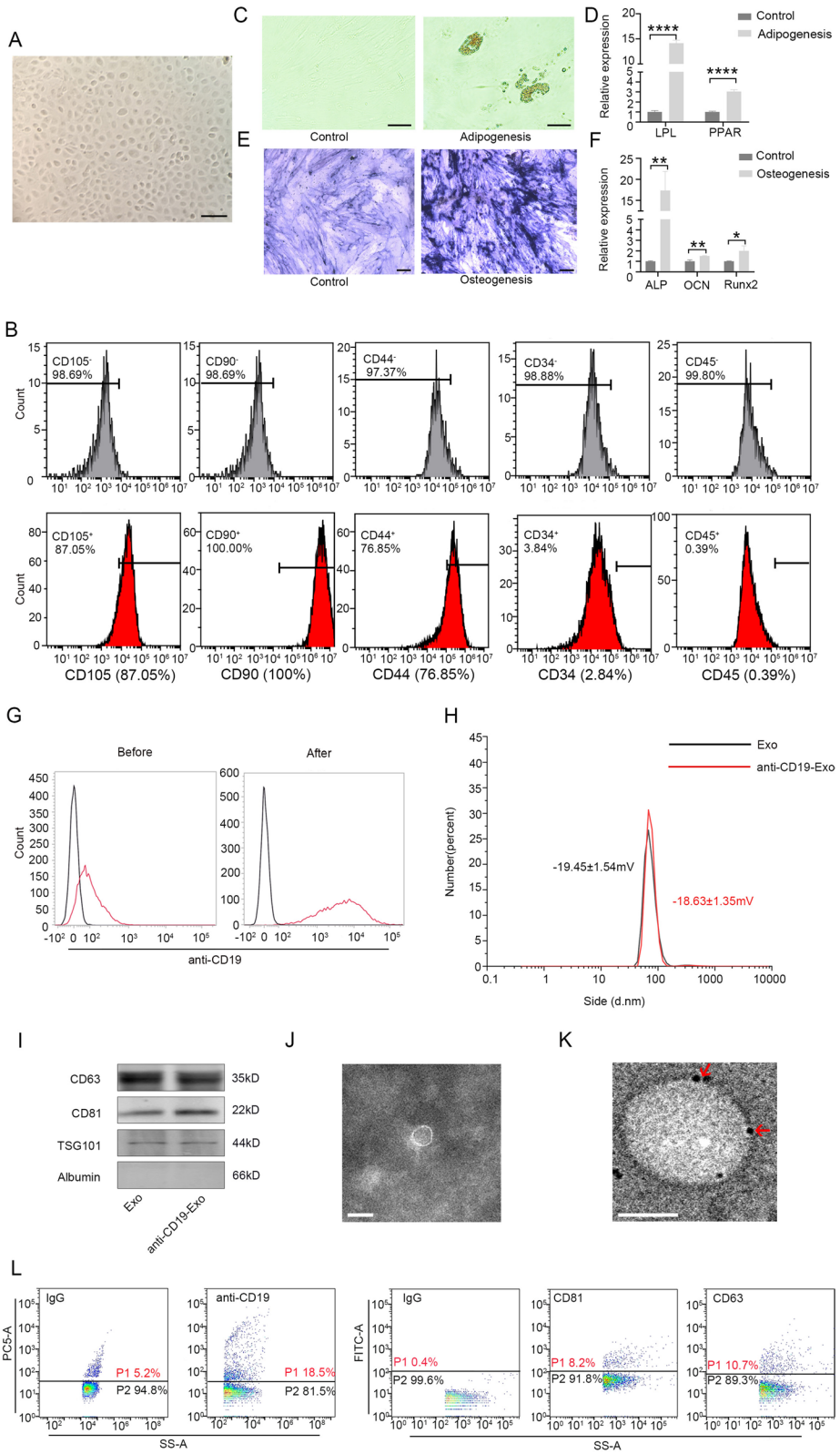

Fig. 1 (See legend on previous page.)

the threshold determination for the experimental group cell populations, based on control cells, are presented in Additional File 1 Figure S1D, E and Figure S2A–D.

The synthesis of anti-CD19-Exo-MTX

MTX (500 μg) was added into 1mL of PBS including anti-CD19-Exo (1 mg) and incubated in a constant temperature shaking at 37 °C for 24 h. The mixture was purified using an ultrafiltration tube with molecular weight cut-off of 100 kDa (Millipore) for 5 times (2500 r/min) to remove of unloaded drugs and obtain anti-CD19-Exo-MTX. The content of MTX in exosomes was determined by high performance liquid chromatography (HPLC; Agilent Technologies). Anti-CD19-Exo-MTX was added with DMSO and thoroughly mixed, after ultrasound, centrifuging at 16,500×*g* for 20 min. The supernatant was detected by HPLC. The supernatant was filtered with a 0.22 μm syringe filter and 20 μL aliquots were transferred into HPLC autosampler vials. The drug loading efficiency and encapsulation efficiency of MTX was calculated using the following equations [27]:

$$\begin{aligned}&\text{Loading efficiency}\\&=\left(\text{weight of the encapsulated MTX}\right)\\&\quad/\left(\text{weight of anti - CD19 - Exo - MTX}\right)\\&\quad\times 100\%,\ \text{encapsulation efficiency}\\&=\left(\text{weight of the encapsulated MTX}\right)\\&\quad/\left(\text{weight of the total MTX added}\right)\times 100\%.\end{aligned}$$

Exosome labeling and uptake

Exosomes were labeled using DiR Iodide (Yeasen) and PKH67 (Sigma-Aldrich) according to the manufacturer's instructions. In brief, exosomes were incubated for 30 min with DiR dye at 37 °C, or at room temperature with PKH67 dye for 5 min, terminated with FBS followed by centrifugation at 100,000×*g* for 2 h at 4 °C. The pellet was resuspended in PBS and subsequently centrifugated at 100,000×*g* for another 2 h.

Subsequently, the MTX-loaded exosomes labeled with PKH67 were incubated with SU-DHL-8 cells for 24 h. Some of the cells were then fixed and stained with β-actin and 4′,6-diamidino-2-phenylindole (DAPI, 40727ES10, Yesen). Images were obtained on a confocal microscope. The fluorescence intensity of intracellular exosomes was quantitatively determined by FCM to assess the cellular uptake.

Intracellular MTX accumulation

To quantify the amount of MTX accumulation in lymphoma cells, anti-CD19-Exo-MTX was added in and incubated with SU-DHL-8 cells for 6, 12 or 24 h, then the cells were collected to be resuspended in PBS before subjected to cell counting. The counted cells were disrupted by an ultrasonic method. The precipitation was removed using a 0.22 μm syringe filter, and the supernatant was measured by using HPLC to determine the concentrations of MTX.

Drug release

The in vitro release behavior of MTX from anti-CD19-Exo-MTX was investigated using a dialysis method. MTX was used as the control groups. 1 mL anti-CD19-Exo-MTX (100 μg MTX) in a dialysis bag (3500Da, MWCO), followed by dialysis in 10mL medium (PH 7.4) for further incubation at 37 °C with gentle shaking. 1 mL medium was collected at 0.5, 1, 2, 4, 8, 12, 24 and 48 h, followed by adding 1 mL fresh medium. Finally, the released amounts of MTX in the collected media were measured using HPLC.

TEER measurement

To monitor cell confluence and the development of tight junctions, transendothelial electrical resistance (TEER) was recorded using a Millicell ERS-2 Voltohm-meter (Millipore, MA, USA) [28]. One electrode was placed on the luminal side and the other electrode on the abluminal side with the endothelial layer separating them. The TEER measurements of blank filters (without cells) were subtracted from those of filters with cells. Then the resulting value was multiplied by the membrane area to obtain the TEER measurements in $\Omega.cm^2$. The formula is as follows: TEER ($\Omega \times cm^2$) = (resistance of co-cultured cells - resistance of empty Transwell filter) × surface area (cm^2).

Permeability assay

The permeability of BBB was evaluated by measuring the clearance of sodium fluorescein (NaFl, 376.3 Da, Sigma-Aldrich), as described previously [29]. Briefly, NaFl was added to the upper compartment of Transwel inserts at a concentration of 100 μg/mL. Medium samples were collected from the bottom well at 30, 60, and 120 min to measure the fluorescence intensity, using a Synergy NEO (BioTek). All experiments were performed in triplicate for each condition. Transendothelial permeability coefficient (Pe) was calculated as previously described by Deli et al. [30, 31].

Investigation of the mechanism of blood-brain barrier penetration in vitro

Each group of drugs was added to the model and the MTX concentration in the model was determined at time points (1, 2, 4, 6, 8, 12, 24 and 48 h) to assessing the permeability of drugs across the BBB. To determine the

integrity of the endothelial monolayer, 10 kDa CY5-dextran, and 70 kDa fluorescein isothiocyanate (FITC)-dextran were added to the upper chamber of the Transwell filters (100 μg/mL), and the fluorescence intensity in the media of the lower chamber was measured after 2 h using a Synergy NEO (BioTek).

In this model, the cells were fed with endothelial growth media supplemented with 8-(4-chlorophenylthio)-adenosine 3′,5′-cyclic monophosphate (8-CPT-cAMP, 50 nM, HY-134299 MCE) and 4-(3-butoxy-4-methoxybenzyl)-2-imidazolidinone (Ro20-1724, 17.5 nM, E0346 selleck). After 48 h, confirmation of increased expression of ZO-1 protein in endothelial cell tight junctions through changes in permeability measured by confocal microscopy and dextran diffusion.

To evaluate the transport pathway of anti-CD19-Exo-MTX using this model with SU-DHL-8 cells were cultured in the lower chamber, filters were pretreated with Dynasore (100 μM, S9849 selleck) and 5-(N-Ethyl-N-isopropyl)- Amiloride (EIPA) (100 μM, S9849 selleck) for 30 min prior to adding the Dir-labeled anti-CD19-Exo-MTX and then incubated for 24 h at 37 °C. The fluorescence intensity of intracellular exosomes in the lower chamber was quantitatively determined by FCM to assess permeability of anti-CD19-Exo-MTX.

In vivo model of CNSL

Animals were housed and maintained in accordance with the institutional guidelines for the use of laboratory animals and after acquiring permission from the ethics committee of Soochow University for animal experimentation. SU-DHL-8 cells (1×10^6 cells per mouse) were subcutaneously inoculated into the left axilla, and lymphoma tumor tissues were harvested to prepare tumor tissue suspensions after two weeks. The mouse model of CNSL was established by intracranial positioning technique. After anesthesia, animals were fixed into the stereotactic headframe, disinfected, cut along the midline of the mouse's head with the length of about 5 mm and 1.5 mm bur hole was drilled 1 mm anterior to the coronal suture on the left hemisphere and 2 mm lateral from the midline. 4 μL SU-DHL-8 cell tissue suspension (1×10^6 cells per mouse) which from NOD-scid mice was injected into the left frontal lobe of the brain. Bone wax filled the skull hole and the incision was sutured. Tumor size and location were monitored by T_2-weighted Magnetic resonance imaging (MRI) on an MRS 3000 scanner (3T).

Antitumor efficacy of anti-CD19-Exo-MTX in CNS lymphoma mouse model

Six-week-old female NOD-scid mice were purchased from a biocytogen company (Beijing, China), and were acclimated one week prior to tumor cell inoculation. CNSL mice models were established, and assigned each mouse a number, then used a random number table to allocate 5 mice to each group: (1) Control group: intravenous (i.v.) injection of 100 μL PBS, (2) MTX group: i.v. injection of 5 mg/kg MTX (100 μL), (3) Exo-MTX group: i.v. injection of 100 μL Exo-MTX (equivalent to 5 mg/kg MTX), (4) anti-CD19-Exo-MTX group: i.v. injection of 100 μL anti-CD19-Exo-MTX (equivalent to 5 mg/kg MTX). Formulations for the different treatment groups were administered every two days, for a total of 7 doses. During the evaluation, the mice were monitored daily for body weight and tumor volume by Magnetic resonance imaging (MRI, MRS-3031, UK) on day 7 and 14.

Targeted distribution of anti-CD19-Exo-MTX in vivo

DiR-labeled Exo-MTX and anti-CD19-Exo-MTX (equivalent to 5 mg/kg MTX) were administrated into the CNSL mice via tail vein injection. The fluorescence distribution was photographed by the IVIS Lumina III optical imaging system (USA) at 1, 6, 12, 24, and 48 h post-administration. The mice were euthanized at 48 h-post administration and their brains and the other major organs were collected to analyze the biodistribution of DiR-labeled Exo-MTX and anti-CD19-Exo-MTX using the IVIS imaging system.

MTX quantification

The MTX solutions with concentrations of 12.5, 25, 50, 100, and 200 μM were then added to the HPLC instrument. Chromatographic conditions: Column: C18 column (Extend-C18, 250 × 4.6 mm, 5 μm; Agilent Technologies); Mobile phase: Water-acetonitrile (90:10); Flow rate: 1 mL/min; UV detection wavelength: 302 nm; Temperature: 25 °C; Injection volume: 20 μL.

Pharmacokinetic studies

Five mice each group were sacrificed at 0.5, 1, 2, 4, 6, 8, 12, 24 and 48 h after intravenous administration of MTX and anti-CD19-Exo-MTX at a dose of 5 mg/kg MTX. The blood was collected and centrifuged at 4000 rpm for 10 min to obtain the plasma. About 100 μL of the supernatant plasma was mixed with 50 μL of methanol, then 50 μL of trichloroacetic acid was added. The mixture was vortexed for 5 minutes and left to stand at 4 °C for 12 h to precipitate the plasma proteins. Then centrifuged at 12,000 rpm for 15 min at 4 °C. The supernatant was withdrawn and filtered through a 0.22-μm polyvinylidene difluoride membrane. MTX levels in blood were quantified by first establishing a standard calibration curve using the previously described method, followed by measuring the processed blood samples via HPLC.

Blood–brain barrier permeability assessment in vivo

PBS, MTX, Exo-MTX and anti-CD19-Exo-MTX were intravenously injected into the CNSL mice at the dose of 5 mg/kg MTX respectively. After 24 h, blood and cerebrospinal fluid (CSF) samples were collected from different treatment groups mice after anesthesia, all mice were euthanized. After euthanasia, brain tissue was removed, weighed, and homogenized in 1.5 mL physiological saline. Then, chloroform and methanol were added, vortexed for 5 min, and centrifuged at 3000 rpm for 10 min. The lower chloroform layer was collected, evaporated in a fume hood, and re-dissolved in 50 μL DMSO. The concentration of MTX in blood, CSF and brain tissue were determined using HPLC.

LC-MS/MS analysis

The hAMSC-Exo samples were subjected to ultrasonic lysis, and 5 μL of the sample was taken for silver staining. After silver staining, the samples were subjected to enzymatic digestion, and the volume was adjusted to a consistent level with lysis buffer. Dithiothreitol (DTT, Sigma-Aldrich) was then added to a final concentration of 5 mM, and the mixture was reduced at 56 °C for 30 min. Iodoacetamide (IAM, Sigma-Aldrich) was subsequently added to a final concentration of 11 mM, and the samples were incubated in the dark at room temperature for 15 min. TEAB (Sigma-Aldrich) was used to dilute urea to ensure the final concentration was below 2 M. Trypsin (Promega) was added at a 1:50 ratio for overnight digestion, followed by a second addition of trypsin at a 1:100 ratio for a further 4 h of digestion. The peptides were dissolved in mobile phase A for liquid chromatography and separated using the ultrahigh-performance liquid chromatography system (EASY-nLC 1200). Mobile phase A consisted of water with 0.1% formic acid (Fluka) and 2% acetonitrile (ThermoFisher Scientific), while mobile phase B contained water with 0.1% formic acid and 90% acetonitrile. The liquid chromatography gradient was set as follows: 0–68 min, 6–23% B; 68.0–82.0 min, 23–32% B; 82.0–86.0 min, 32–80% B; 86.0–90.0 min, 80% B, with a flow rate of 500 nL/min. After separation, the peptides were introduced into the NSI ion source for ionization and analyzed using the Orbitrap Exploris™ 480 (ThermoFisher Scientific) mass spectrometer. The ion source voltage was set to 2.3 kV, with FAIMS compensation voltages (CV) of −45 and −65 V. Both parent ions and their secondary fragments were detected and analyzed using high-resolution Orbitrap detection.

Statistical analysis

All statistical analyses were performed using GraphPad Prism 8.0. All data were shown as mean ± SEM. For normally distributed data, the significance of mean differences was determined using unpaired two-tailed Student's *t*-test between two groups or ANOVA followed by Newman-Keuls multiple comparison test among multiple groups. For all tests, a p-value < 0.05 was considered to be statistically significant.

Other detailed assays including isolation, culture and identification of hAMSCs, targeting experiment in vitro, in vitro model of BBB, cell viability assays, the complete blood count and serum biochemistry assay, H&E and Ki67 staining, TUNEL and Nissl staining are available in the Additional file 2.

Results

Characterization of hAMSCs and the preparation of hAMSCs-derived anti-CD19-Exo

hAMSCs isolated from human adipose tissue exhibited a distinctive spindle-shaped morphology (Fig. 1A). Flow cytometry analysis further confirmed their identity by revealing positive expression of established MSC markers, including CD105, CD44, and CD90 (Thy-1), while demonstrating negativity for hematopoietic cell markers CD34 and CD45 (Fig. 1B). Oil Red O staining demonstrated the substantial accumulation of lipid droplets after 14 days in the MSC adipogenesis differentiation medium (Fig. 1C). Concurrently, the expression levels of key lipogenic genes, such as Lipoprotein Lipase (LPL) and Peroxisome Proliferator-Activated Receptor (PPAR), exhibited significant increases (P < 0.001) (Fig. 1D). BCIP/NBT Alkaline Phosphatase staining showed pronounced calcium salt deposition in the MSC osteogenesis differentiation medium after 14-day period (Fig. 1E), accompanied by significant upregulation of osteogenic genes Alkaline Phosphatase (ALP), Osteocalcin (OCN), and Runt-related transcription factor 2 (Runx2) (P < 0.05) (Fig. 1F). These results provided evidence of the adipogenic and osteogenic differentiation capabilities of hAMSCs. Consequently, these results confirmed the successful isolation of hAMSCs.

We next aimed to utilize the natural targeting properties of exosomes derived from hAMSCs to specifically deliver therapeutic cargo to CNSL. CD19 is considered an excellent target for immunotherapy in B-cell lymphoma. We introduced the lentiviral vector containing the anti-CD19 construct into hAMSCs, and then employed flow cytometry-based sorting to identify and isolate the significant fraction of cells expressing the anti-CD19 (Fig. 1G). Then we collected exosomes secreted by the engineered hAMSCs and characterized the exosomes using Dynamic light scattering analysis (DLS), western blotting and transmission electron microscopy (TEM) to confirm their size, presence of exosome markers and morphology. The size of the unmodified exosomes ranged from 40 to 120 nm, and the zeta potential was

−19.45±1.54 mV, anti-CD19 modification maintain the particle size distribution of the exosomes without changing the zeta potential (Fig. 1H). The unmodified exosome and anti-CD19-Exo were positive for the exosome marker proteins CD63, CD81 and TSG101, and did not expressed albumin, the negative marker of exosome (Fig. 1I). Anti-CD19-Exo was spherical vesicle with a double-layered membrane structure, as verified by TEM (Fig. 1J). Additionally, anti-CD19 was strongly expressed in engineered hAMSCs, incorporated into the hAMSCs-derived exosomes, and was identified on the external surface of the exosomes based on colloidal gold immunoelectron microscopy (Fig. 1K) and flow cytometry (Fig. 1L). Collectively, we conducted a characterization of hAMSCs and generated anti-CD19-Exo derived from them.

Development and evaluation of anti-CD19-Exo-MTX for lymphoma targeted drug delivery

To quantify MTX, MTX solutions of different concentrations were prepared, and a standard calibration curve was constructed. The equation relating peak area (Y) to concentration (C) is: $Y = 27.103C - 35.439$ ($R^2 = 0.9993$). Based on the properties of MTX, we employed co-incubation to load MTX into anti-CD19-Exo. Loading efficiency and encapsulation efficiency are commonly used parameters to evaluate the efficiency of drug loading into exosomes or other drug delivery systems [27]. We controlled the quality of exosomes and increased the dosage of MTX. When the drug-to-exosome ratio was 1:2, the highest drug loading efficiency and encapsulation efficiency were achieved. The anti-CD19-modified exosome-loaded methotrexate (anti-CD19-Exo-MTX) achieved a loading efficiency of 4.24% ± 1.20% and an encapsulation efficiency of 9.05% ± 4.50% measured by HPLC when the dosage of exosomes was 1 mg/mL (Fig. 2A). This loading process had no discernible impact on the physical characteristics of the exosomes, as confirmed through DLS, western blotting, and TEM analyses (Fig. 2B-D). Furthermore, infrared spectroscopy analysis unveiled distinctive absorption peaks at 2976 and 3249 cm^{-1}, which were clear indicators of the presence of methyl and amido groups, both characteristic constituents of MTX specific chemical structure (Fig. 2E). These results unequivocally confirmed the effective encapsulation of MTX within anti-CD19-Exo. The particle size and zeta potential of anti-CD19-Exo-MTX stored at −80 °C for long-term storage exhibited excellent stability (Additional file 1 Figure S1B). To assess the potential uptake of anti-CD19-Exo-MTX by lymphoma cells, PKH67-labeled anti-CD19-Exo-MTX was introduced to SU-DHL-8 cells. The ability of SU-DHL-8 cells to internalize anti-CD19-Exo-MTX was confirmed via flow cytometry (Fig. 2F) and immunofluorescence assays (Fig. 2G). For a comprehensive evaluation of cellular uptake and drug delivery, we conducted a quantitative comparison of drug accumulation within lymphoma cells, both for the free drug and the exosome-loaded drug, utilizing HPLC. In SU-DHL-8 cells, at 6 h, the intracellular MTX concentration was higher in anti-CD19-Exo-MTX group than in the free MTX group ($P < 0.05$). This trend not only persisted but also intensified after 24 h (Fig. 2H). Additionally, the assessment drug release from exosomes provides valuable insights into drug delivery kinetics and the potential for sustained drug release [32]. To achieve this, MTX-loaded exosomes were separated from the release medium using a dialysis membrane and filtration techniques, with a pH of 7.4 employed to simulate the physiological pH levels of blood. As depicted in Fig. 2I, the cumulative release of anti-CD19-Exo-MTX exhibited a slower rate compared to free MTX ($P < 0.01$), underscoring the efficacy of anti-CD19-Exo as a drug delivery system with controlled release properties. Next, we examined the specific binding capability of anti-CD19-Exo-MTX to DLBCL cells expressing CD19 on their cell surface. Flow cytometry assays demonstrated that anti-CD19-Exo-MTX selectively bound to the surface of SU-DHL-8 cells, while it did not bind to 293T cells, which lacked CD19 expression on their cell surface (Fig. 2J). We successfully developed anti-CD19-Exo-MTX as an efficient drug delivery system for targeting lymphoma cells.

(See figure on next page.)

Fig. 2 Preparation and characterization of anti-CD19-Exo-MTX. **A** The loading efficiency and encapsulation efficiency of different concentrations of MTX into hAMSCs-derived exosomes. **B** Zeta potential and size distribution of hAMSCs-derived exosomes and anti-CD19-Exo-MTX were determined by DLS. **C** CD63, CD81, TSG101 and Albumin of exosomal markers were detected in hAMSCs-derived exosomes and anti-CD19-Exo-MTX by Western blot assay. **D** Representative image of anti-CD19-Exo-MTX via TEM (Scale bar, 100 nm) and immunogold microscopy (Red arrows indicate colloidal gold particles, scale bar, 50 nm). **E** The loading of MTX into exosomes was detected by infrared spectroscopy. **F, G** Internalization was measured by flow cytometry (**F**) and immunofluorescence assays (Scale bar, 20 μm) (**G**), after co-incubating anti-CD19-Exo-MTX and SU-DHL-8 cells for 24 h. **H** Intracellular MTX accumulation of SU-DHL-8 treated with free MTX and anti-CD19-Exo-MTX after incubation for 6, 12 and 24 h. **I** Cumulative release of MTX and anti-CD19-Exo-MTX behaviors at pH 7.4 by HPLC. **J** Flow cytometry was employed to assess the targeting specificity of anti-CD19-Exo-MTX in vitro. Data are shown as mean ± SEM, and the experiment was performed three times and a representative example is shown. **H**, **I** and **J** were analyzed by unpaired two-tailed Student's *t*-test. *$P < 0.05$, **$P < 0.01$, ***$P < 0.001$, ****$P < 0.0001$

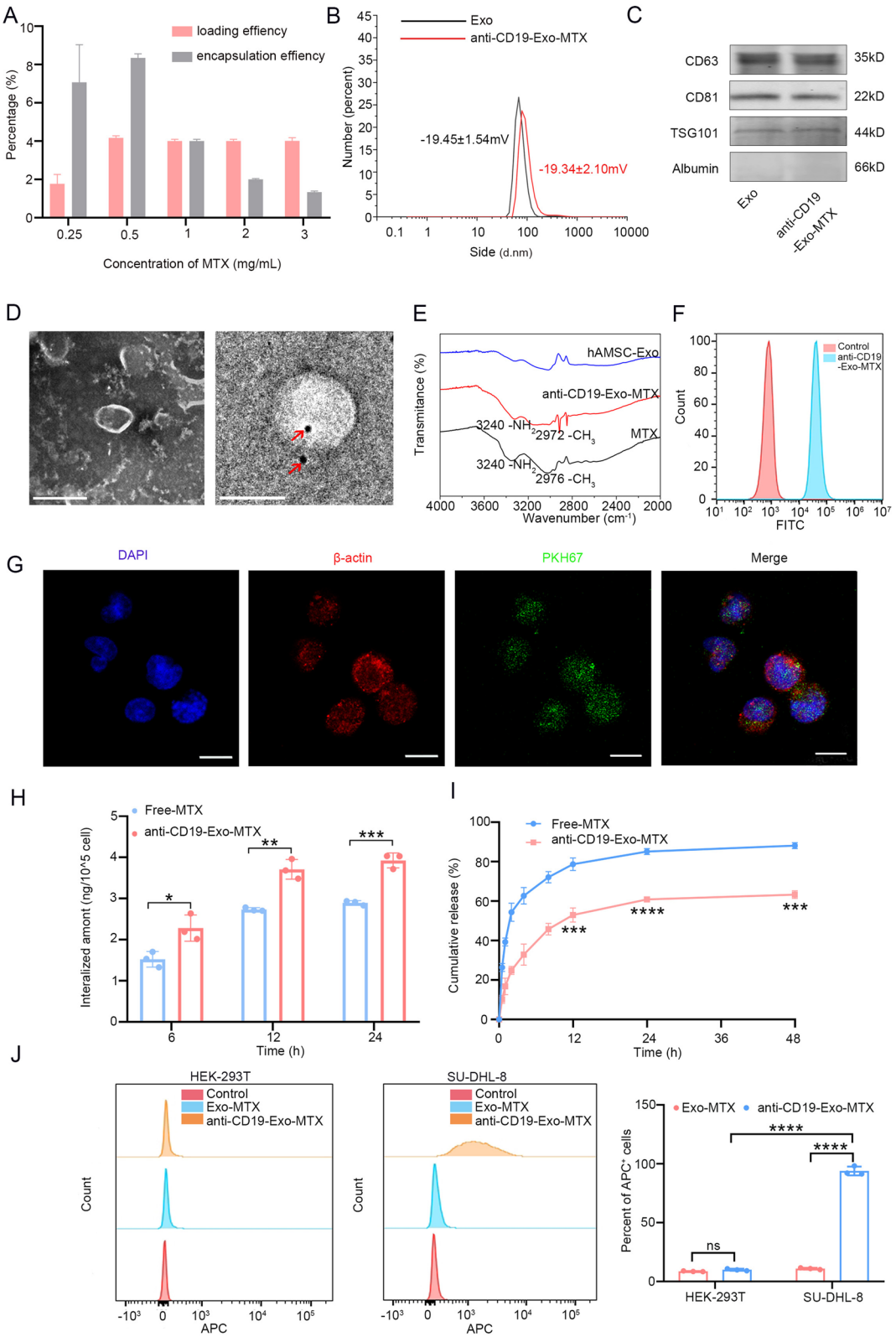

Fig. 2 (See legend on previous page.)

Anti-CD19-Exo-MTX crosses the blood–brain barrier

We constructed an in vitro model of the BBB using brain vascular endothelial cell hCMEC/D3 and human astrocytes (Fig. 3A, left panel). Neither of them expressed CD19 (Additional file 1 Figure S1F). Transendothelial electrical resistance (TEER) measurements were utilized to assess the integrity and suitability of the model for in vitro experiments (Fig. 3A, right panel). When investigating the barrier permeability by NaFl (376.3 Da), showing appropriate permeability of BBB (Additional file 3 Table 3)[29].It was evident that, relative to free MTX, anti-CD19-Exo-MTX exhibited superior transmigration across the BBB at different time points ($P < 0.001$). No significant difference in permeability was observed between the anti-CD19-Exo-MTX and Exo-MTX (Fig. 3B). Moreover, anti-CD19-Exo-MTX crossed the BBB model without compromising its structure, as assessed by the luminescent signal assay of dextran (Fig. 3C).

Subsequently, we delved into the mechanism by which exosomes traverse the BBB, specifically exploring whether it occurs through the surrounding extracellular space or transcytosis. We treated hCMEC/D3 with a combination of cAMP and Ro20-1724, known to reinforce cell junctions by regulating junctional proteins like ZO-1 (Fig. 3D), thereby enhancing the barrier function (Fig. 3E). After treating hCMEC/D3 with cAMP and Ro20-1724 for 48 h, SU-DHL-8 cells were added to the lower chamber, and DiR-labeled anti-CD19-Exo-MTX was added to the upper chamber. After 24 h, SU-DHL-8 cells were collected and flow cytometry was used to measure the uptake of anti-CD19-Exo-MTX by SU-DHL-8. Notably, the luminescent signal of DiR detected in cAMP-Ro20-1724 treated group remained consistent when compared to the control group (Fig. 3F). This suggested that the mechanism by which anti-CD19-Exo-MTX crossed the BBB did not appear to involve movement through the surrounding extracellular space. We also utilized EIPA, a potent and specific inhibitor of Na+/H+ exchanger activity essential for macropinosome formation [33, 34]. Pre-treatment with EIPA revealed no significant change in the luminescent signal, indicating that the passage of anti-CD19-Exo-MTX across the BBB was not facilitated by micropinocytosis (Fig. 3F). In contrast, Dynasore is an inhibitor of dynamin, a GTPase protein that plays a key role in clathrin-mediated endocytosis, and effectively hinders coated vesicle formation [35]. Pre-treatment with Dynasore resulted in a noteworthy decrease in the luminescent signal ($P < 0.001$) (Fig. 3F), strongly suggesting that anti-CD19-Exo-MTX traversed the BBB via receptor-mediated endocytosis. These data demonstrated the effective transmigration of anti-CD19-Exo-MTX across the BBB.

Anti-CD19-Exo-MTX improves CNSL proliferation inhibition

We proceeded to assess the capacity of anti-CD19-Exo-MTX to inhibit CNSL proliferation. Anti-CD19-Exo-MTX and an equivalent dose of free MTX were introduced into the upper chamber of Transwell filters, respectively. Anti-CD19-Exo loaded MTX exhibited a more potent suppressive effect when compared to free MTX after crossing the BBB ($P < 0.01$) (Fig. 4A). Meanwhile, Anti-CD19-Exo or exosome alone did not exhibit inhibition of SU-DHL-8 cell proliferation (Fig. 4B, Additional file 1 Figure S1C). Moreover, colloidal gold immunoelectron microscopy showed that anti-CD19-Exo-MTX retained its intact morphology and anti-CD19 modification after crossing the BBB (Fig. 4C).

To evaluate the efficacy of anti-CD19-Exo-MTX in vivo, intracranial orthotopic CNSL models in mice were established, with 5 mice per group (Fig. 4D). CD20 immunohistochemistry confirmed the intracranial tumor in the left frontal lobe of the brain (Fig. 4E). Magnetic resonance imaging (MRI) analysis revealed a reduced disease burden in the anti-CD19-Exo-MTX group compared to both the MTX and Exo-MTX groups (Fig. 4F, G), along with prolonged overall survival ($P < 0.05$) (Fig. 4H). Intracranial mouse models in each group resulted in cachexia symptoms, characterized by anorexia, muscle wasting, and overall weight loss. Notably, the anti-CD19-Exo-MTX group showed a milder presentation of cachexia, with minimal body weight loss compared to the

(See figure on next page.)

Fig. 3 Anti-CD19-Exo-MTX crossed the in vitro BBB model. **A** Schematic illustration of an in vitro BBB model co-cultured with hCMEC/D3 and HA cell lines. Mean TEER values over 10 days for in vitro BBB model. **B** The transportation ratio of MTX across the blood-brain barrier model observed at different time points after application of MTX, Exo-MTX and anti-CD19-Exo-MTX. **C** Mean fluorescence intensity of 10 kDa CY5-dextran and 70 kDa FITC-dextran in media of the lower chambers of the BBB model following application of PBS, exosomes, MTX, Exo-MTX and anti-CD19-Exo-MTX. **D** Fluorescent microscopy images of junctional protein ZO-1 in hCMEC/D3 before and after treatment of cAMP and RO20-1724 for 48 h. Scale bar, 50 μm. **E** Fold change in permeability coefficient of hCMEC/D3 to 10 kDa CY5-dextran and 70 kDa FITC-dextran following treatment with cAMP and Ro20-1724 for 48 h. **F** The change in fluorescent signal uptake of DiR-labeled anti-CD19-Exo-MTX in SU-DHL-8 cells from the lower chambers of the BBB model after treatment with Dynasore, EIPA, cAMP, and Ro20-1724. Data are shown as mean ± SEM, and the experiment was performed three times and a representative example is shown. **B**, **E** and **F** were analyzed by unpaired two-tailed Student's *t*-test. ns, no significant, $^{*}P < 0.05$, $^{**}P < 0.01$, $^{***}P < 0.001$, $^{****}P < 0.0001$

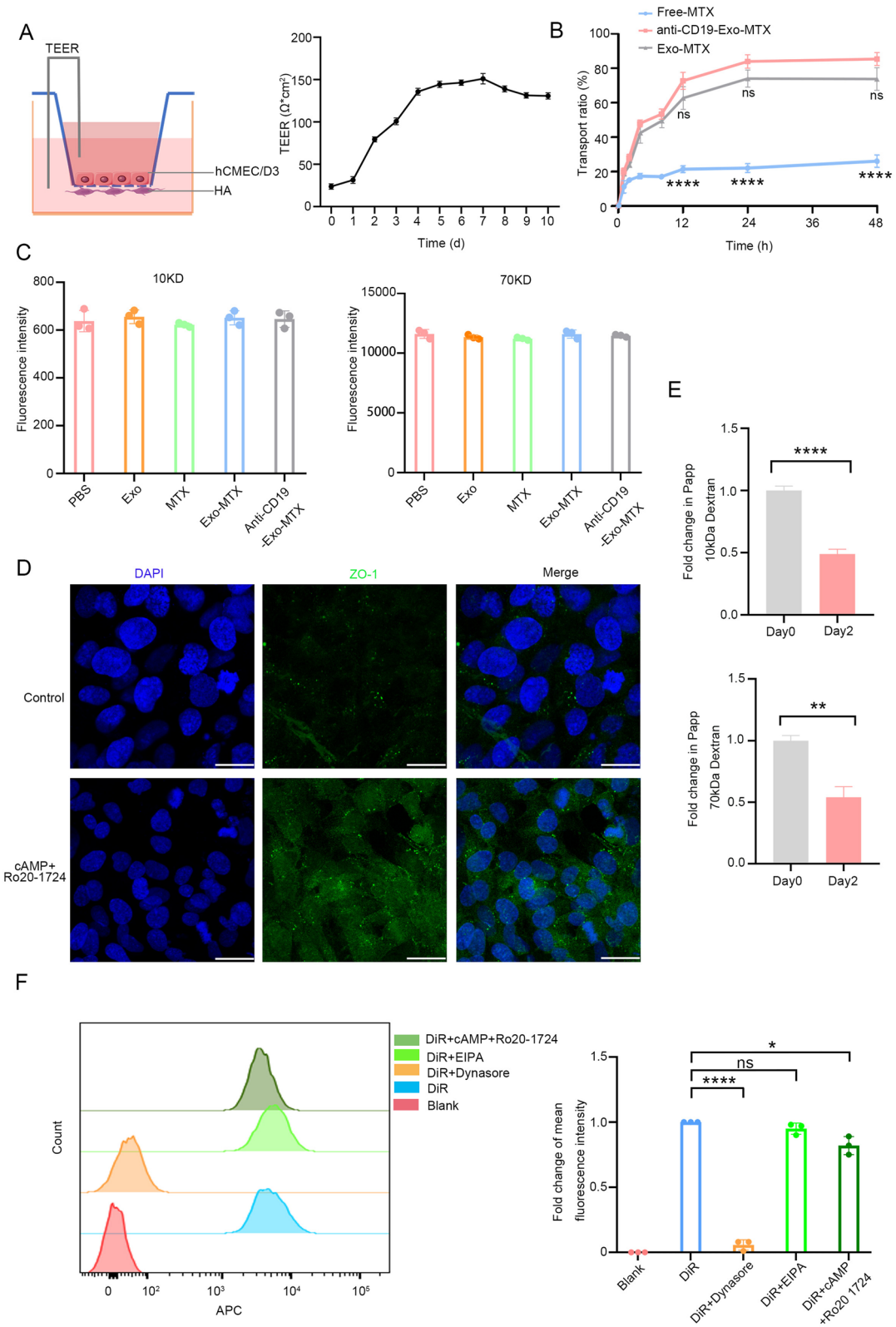

Fig. 3 (See legend on previous page.)

other groups ($P < 0.05$) (Fig. 4I). The pharmacokinetic studies indicated that anti-CD19-Exo-MTX exhibited higher concentrations and extended blood circulation time compared to free MTX ($P < 0.01$) (Fig. 4J). Drug concentration analysis in the CSF and brain tissue demonstrated enhanced stability and longer-lasting drug levels for anti-CD19-Exo-MTX in the CSF and brain tissue ($P < 0.01$) (Fig. 4K). The Ki-67 proliferation index of the tumor indicated that anti-CD19-Exo-MTX more effectively suppressed CNSL ($P < 0.05$) (Fig. 4L).

To assess biodistribution and targeting of anti-CD19-Exo-MTX, exosomes were labeled with Vivo Track DiR (Fluorescence). A strong fluorescence signal was observed primarily within the intracranial region for anti-CD19-Exo-MTX, while Exo-MTX exhibited a broader systemic distribution (Fig. 4M, N). Forty-eight hours post-injection, organ removal revealed heightened fluorescence signals in the brain and diminished signals in the liver, kidney, and lung for anti-CD19-Exo-MTX, affirming its targeted delivery of MTX to CNSL in vivo (Fig. 4O). Collectively, anti-CD19-Exo-MTX demonstrated potent in vitro and in vivo therapeutic efficacy against CNSL, resulting in decreased disease burden, prolonged overall survival, and enhanced drug targeting.

The mitigating effect of exosomes on the toxic side effects induced by MTX

MTX treatment for central nervous system lymphoma can induce diverse toxic side effects, including neurotoxicity, hepatic and renal impairment, mucosal damage and myelosuppression [1, 4, 36]. Exosomes carry various bioactive molecules, with proteins playing a crucial role. By transporting proteins, exosomes can achieve specific interactions with target cells, influencing cellular behavior, regulating signaling pathways, and even altering cell fate [37–39]. To evaluate the cellular effects of hAMSCs-exosomes, we employed Liquid chromatograph - tandem mass spectrometer (LC-MS/MS) for the identification and characterization of exosomal proteins, resulting in the identification of 1245 proteins. The exosomal proteins, engaged in signaling networks governing neuronal development ("Axon development"; "Neuron projection morphogenesis"; "Regulation of neuron projection development"), hepatoprotection ("Liver regeneration"; "Embryonic liver development"; "Liver development"), nephroprotection ("Kidney development"; "Kidney epithelium development"; "Regulation of kidney development"), skin epidermal differentiation ("Skin epidermis development"; "Skin morphogenesis"), and hematopoiesis ("Bone marrow development"), were mapped and visualized using Cytoscape software (Fig. 5A). GO pathway enrichment analysis of signaling pathways revealed significant enrichment in neuron development-related signaling pathways ($P < 0.05$) (Fig. 5B).

We next proceed to experimentally validate neuron development functions of hAMSCs-derived exosome. Terminal deoxynucleotidyl transferase biotin-dUTP nick end labeling (TUNEL) and Nissl staining were performed to detect the histological and pathological changes [40–42]. In the above CNSL mice models, fewer TUNEL-positive cells were observed in anti-CD19-Exo-MTX than in free MTX, demonstrated less apoptosis in mice cerebral cortex ($P < 0.05$) (Fig. 6A, C). Nissl staining was used to detect changes in the hippocampal region of brain tissue. Compared to the free MTX group, mice treated with exosomes as drug delivery vehicles showed an increase in the number of hippocampal neurons ($P < 0.05$) (Fig. 6B, D). This suggested that hAMSCs-derived exosomes partially reversed MTX-induced hippocampal neuronal

(See figure on next page.)

Fig. 4 Inhibition of CNSL proliferation and enhanced targeted delivery by anti-CD19-Exo-MTX. **A** Schematic illustration of the experiment and cell viability of SU-DHL-8 cells in response to treatment with PBS, free MTX (0.05 μM), and anti-CD19-Exo-MTX (equivalent to 0.05 μM MTX) after penetration in the BBB model at 24, 48 and 72 h. **B** Cell viability of SU-DHL-8 cells in response to treatment with different concentrations of anti-CD19-Exo for 24 h. **C** TEM of the anti-CD19-Exo-MTX after penetration in the BBB model (red arrow indicate colloidal gold particles, scale bar, 50 nm). **D** Schematic illustration for experiments with CNSL model mice and treatment. **E** CD20 immunohistochemistry positivity confirmed tumorigenesis. Scale bar, 100 μm. **F** Magnetic resonance imaging (MRI) images and the change of tumor size from different groups of mice before and after treatment on day 7 and 14 (n = 5). **G** Tumor area of MRI after treatment on day 7 (n = 5, mean ± SEM). **H** Kaplan–Meier analysis revealed the survival rate of the mice in experiment (n = 5, mean ± SEM). **I** Body weight curves of CNSL mice after different treatments (n = 5, mean ± SEM). **J** Concentration–time profiles of MTX in blood plasma after intravenous administration of MTX and anti-CD19-Exo-MTX at a dose of 5 mg/kg MTX in NOD-scid mice (n = 5, mean ± SEM). **K** The ratio of MTX concentrations in cerebrospinal fluid to blood (left panel) and brain tissue to blood (right panel) by HPLC at 24 h-post administration of MTX, Exo-MTX and anti-CD19-Exo-MTX at a dose of 5 mg/kg MTX in CNSL mice (n = 5, mean ± SEM). **L** Ki-67 immunohistochemistry staining was employed to assess tumor proliferation at the end of different administration (n = 5, mean ± SEM). **M** Distribution of DiR-labeled Exo-MTX and anti-CD19-Exo-MTX in CNSL mice (n = 3). **N** Quantitative analysis of fluorescent signals in the brain at specific time intervals of 1, 6, 12, 24 and 48 h-post administration (n = 3, mean ± SEM). **O** Biodistribution of DiR-labeled Exo-MTX and anti-CD19-Exo-MTX in the brain, heart, kidney, lung, liver and spleen of the CNSL mice at 48 h-post administration (n = 3). Data are shown as mean ± SEM, and the experiment was performed three times and a representative example is shown. **A, B, G–L** and **N** were analyzed by unpaired two-tailed Student's *t*-test. ns, no significant, *$P < 0.05$, **$P < 0.01$, ***$P < 0.001$, ****$P < 0.0001$

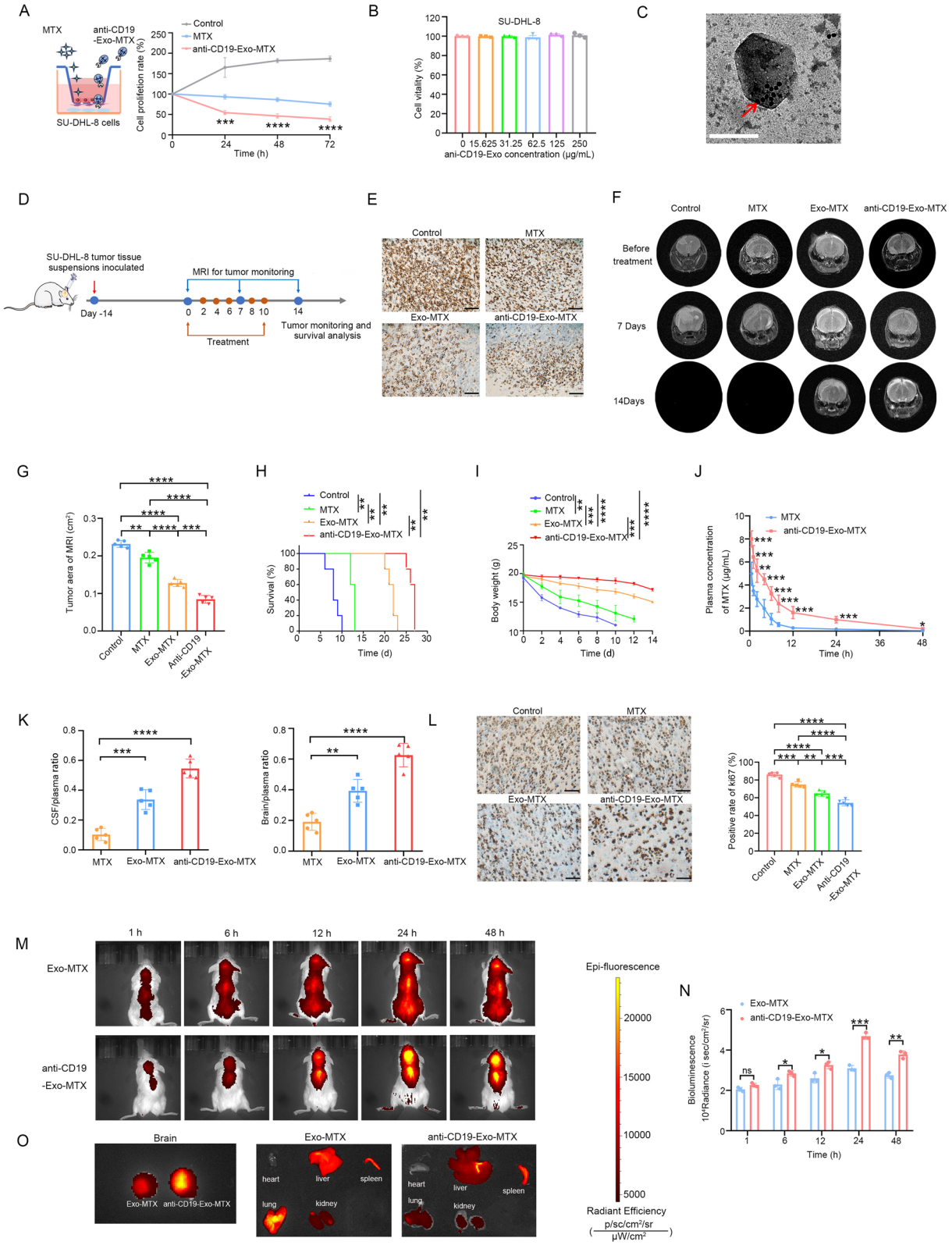

Fig. 4 (See legend on previous page.)

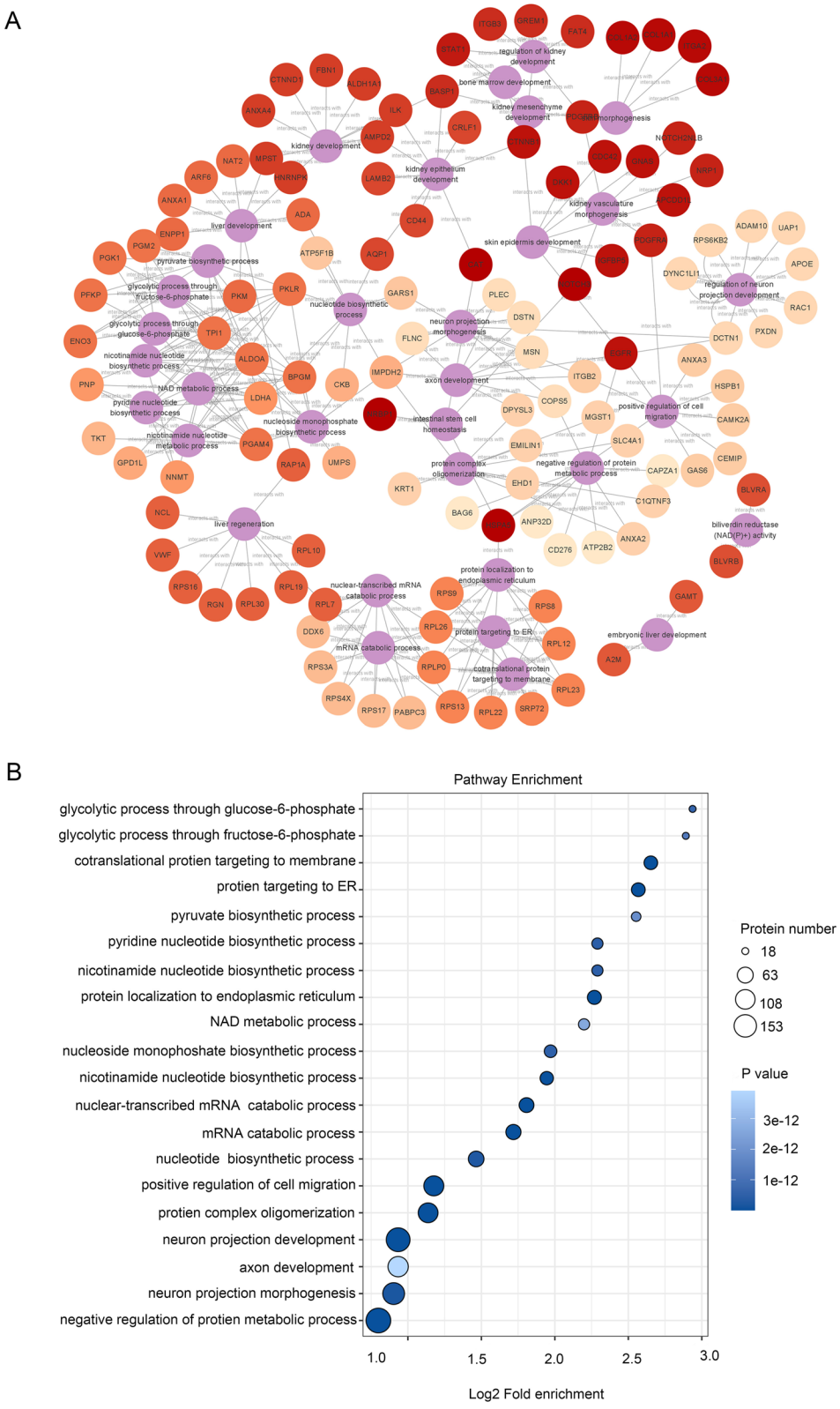

Fig. 5 Proteomic analysis of hAMSCs-derived exosomes. **A** The Cytoscape software was adopted for protein interaction analysis of the protein in hAMSCs-derived exosomes. **B** The protein in hAMSCs-derived exosomes were enriched in pathways

damage, supporting the neuron development functions identified in the LC-MS/MS analysis. Furthermore, in vitro experiments showed that hAMSCs-derived exosomes enhanced the proliferation of the hippocampal neural cell, HT22, confirming their neuroprotective effects (Fig. 6E).

In the CNSL mouse models, we conducted histological examinations of vital organs (Fig. 6F). Firstly, the condition of the liver was assessed. In the MTX-treated group, hepatocytes showed an increased nucleus-to-cytoplasm ratio, partial ballooning degeneration, extensive infiltration of inflammatory cells in the interstitium, vascular dilation, congestion, and focal necrosis. These results indicated MTX-induced liver damage. In the Exo-MTX and anti-CD19-Exo-MTX groups, hepatocytes displayed regular morphology, some hepatocytes exhibited enlarged nuclei with deep staining and high nucleus-to-cytoplasm ratio, occasional binucleated hepatocytes were observed locally, and there was minimal infiltration of inflammatory cells in the interstitium. Furthermore, blood biochemical tests (Additional file 3 Table 1) in mice revealed that in the MTX-treated group, the levels of aspartate aminotransferase (AST) and alanine aminotransferase (ALT) were elevated, whereas in the two groups treated with exosomes, AST and ALT levels were significantly lower than in the MTX-treated group ($P < 0.001$) (Fig. 6G). This suggested that hAMSCs-derived exosomes partially reversed the liver damage caused by MTX.

Next, the condition of the kidney was assessed. As shown in the Fig. 6F, in the MTX-treated group, inflammatory cell infiltration around the glomeruli and renal tubules was observed, accompanied by localized focal necrosis. Conversely, in the Exo-MTX and anti-CD19-Exo-MTX groups, the glomeruli and renal tubules displayed regular morphology, with minimal inflammatory cell infiltration in the interstitium. Furthermore, in the blood biochemistry results, creatinine (CREA), which reflected renal function, was significantly lower in both the Exo-MTX and anti-CD19-Exo-MTX groups compared to the MTX-treated group ($P < 0.001$) (Fig. 6H). Additionally, the inflammatory factor IL-6 was significantly lower in both the Exo-MTX and anti-CD19-Exo-MTX groups compared to the MTX-treated group ($P < 0.001$), further indicating the reversal of hepatic and renal function damage by hAMSCs-derived exosomes (Fig. 6I). Moreover, in vitro experiments showed that hAMSCs-derived exosomes exhibited slight protective effects on the kidney cell HK-2 (Fig. 6J).

In the complete blood count of the animal model mice, abnormalities were observed in white blood cells (WBC), neutrophils (NE), red blood cells (RBC), hemoglobin (HB), and platelet (PLT) levels in the MTX-treated group, whereas in the Exo-MTX and anti-CD19-Exo-MTX groups, these indicators were within normal ranges (Additional file 3 Table 2). This suggested a potential reversal effect of hAMSCs-derived exosomes on MTX-induced myelosuppression. Additionally, in each treatment group of CNSL mouse models, no toxicity or significant histological damage was observed in the heart, spleen, lung, and intestines (Fig. 6F).

Therefore, hAMSCs-derived exosomes, as drug carriers, were safe, and they could partially reverse MTX-induced neurological damage, liver and kidney damage, and myelosuppression.

Discussion

The therapies for CNSL are limited by the biological and pharmacological effects of the BBB [43, 44]. Although MTX plays a key role in the treatment of CNSL, high-dose MTX is essential to penetrate the BBB and achieve anti-tumor effects in the CSF. The clinical application of MTX has been significantly hindered by dose-dependent toxicities, including hepatotoxicity, nephrotoxicity, and neurotoxicity [45]. To address these limitations, we developed an exosome-based delivery system named anti-CD19-Exo-MTX that can be readily produced using hAMSCs as a factory via the endogenous biogenesis of extracellular vesicles (Graphical Abstract).

(See figure on next page.)

Fig. 6 Identifying the function and safety assessment of exosome-based drug carriers. **A** TUNEL assay revealed the level of apoptosis in different treatment groups and **C** fluorescence intensity analysis of TUNEL-positive cells in the hippocampus. Scale bar, 100 μm. **B** Representative images and **D** quantitative data for the number of Nissl-positive hippocampal neurons in different treatment groups. Scale bar, 50 μm. **E** Cell viability of HT22 cells induced injury by MTX in response to treatment with different concentrations of hAMSCs-derived exosomes for 24 h, compared with no exosome group. **F** H&E staining of the tissue of heart, liver, spleen, lung, kidney and intestine in safety evaluation experiments (n = 5, red arrows indicate binucleated hepatocytes, scale bar, 100 μm). **G** The level of the live enzyme of treatment on the intracranial tumor model (n = 5, mean ± SEM). **H** The renal function level of treatment on the intracranial tumor model (n = 5, mean ± SEM). **I** The level of the inflammatory factor IL-6 and TNF-α (n = 5, mean ± SEM). **J** Cell viability of HK-2 cells induced injury by MTX in response to treatment with different concentrations of hAMSCs-derived exosomes for 24 h, compared with no exosome group. Data are shown as mean ± SEM, and the experiment was performed three times and a representative example is shown. **C–E** and **G–J** were analyzed by unpaired two-tailed Student's *t*-test. ns, no significant, *$P < 0.05$, **$P < 0.01$, ***$P < 0.001$, ****$P < 0.0001$

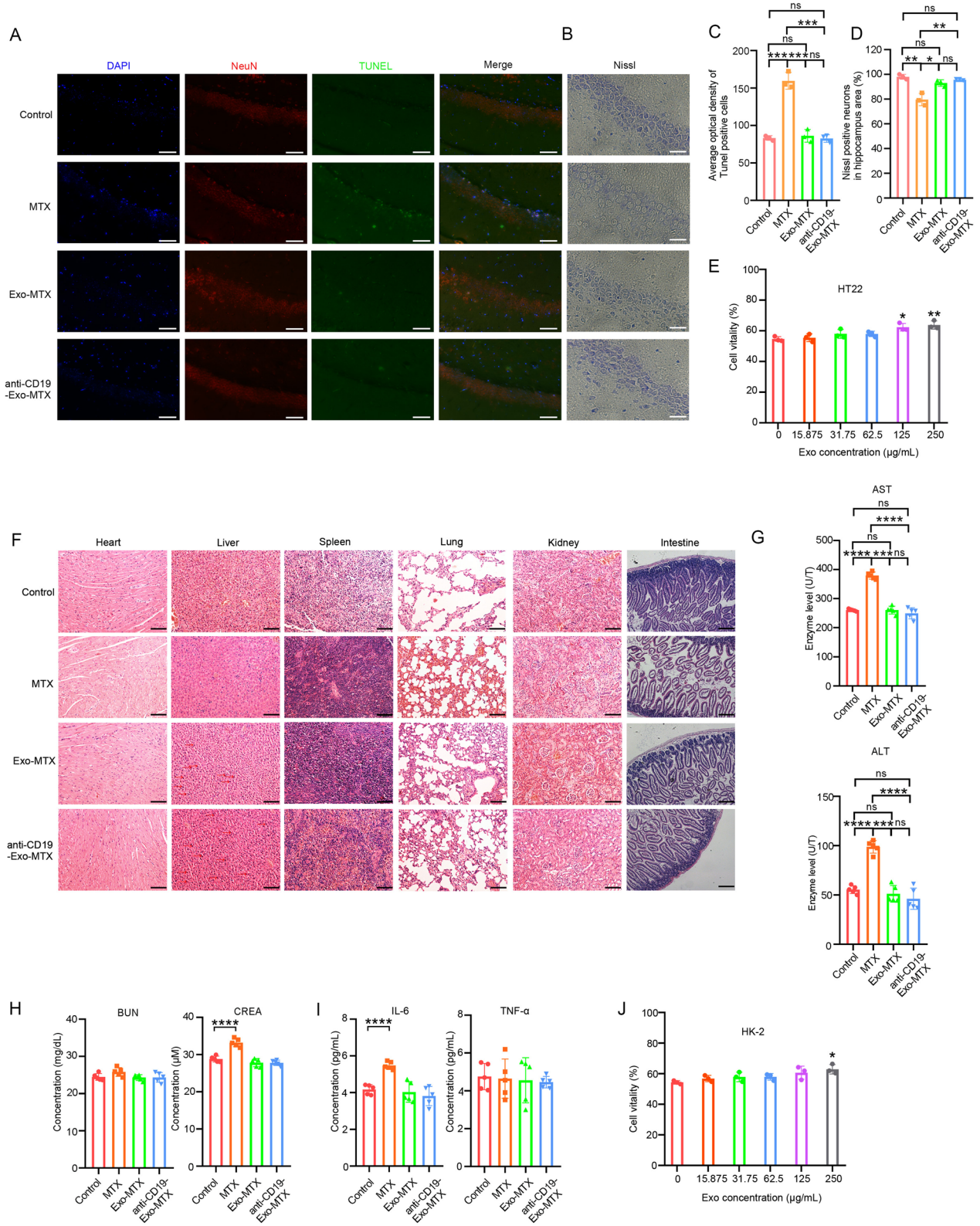

Fig. 6 (See legend on previous page.)

Due to their nano-sized dimensions, bilayer lipid envelope, low immunogenicity, and modifiable properties, exosomes can effectively traverse the BBB and deliver their cargo directly to target cells, making them promising candidates for drug delivery vectors [46]. Choosing the appropriate donor source for exosomes is essential. Most studies tend to use exosomes derived from 293T cells however, since 293T is a tumorigenic cell line, its use in human therapies raises safety concerns [47, 48]. We selected exosomes derived from hAMSCs, encapsulating neurotrophins, immunoregulatory factors, and angiomodulatory factors, exhibited low immunogenicity and neuroprotective properties while crossing the BBB [49–51]. Besides, hAMSCs possess enhanced proliferative capacity, making them more suitable for the large-scale generation of exosomes.

In previous studies on CNSL, encapsulation techniques were commonly employed to load drugs or functional molecules onto specific carriers, enhancing their stability and bioavailability [52]. Building on this foundation, our study incorporates targeted delivery strategies that engineered anti-CD19 into hAMSCs-derived exosomes, which not only preserve the advantages of encapsulation but also improve the specificity of therapeutic delivery to the desired cells or tissues, potentially enhancing therapeutic efficacy while minimizing off-target effects.

Anti-CD19 therapeutic strategies, particularly those targeting B-cell malignancies such as CD19 CAR-T therapy, have already shown clinical success, further validating CD19 as a reliable and clinically relevant target [53, 54]. To specifically deliver MTX-loaded exosomal carriers to lymphoma cells, hAMSCs-derived exosomes were first modified with anti-CD19 before being incubated with MTX to achieve anti-CD19-Exo-MTX. Our results suggested that the surface morphology, particle size, and zeta potential of exosomes remained almost unchanged after modification and MTX encapsulation, indicating the processes of modification and loading did not have adverse effects on the morphological properties and stability of natural exosomes, which also demonstrated long-term storage stability. Considering that the antibody fragment was modified on the surface of exosomes, we opted for drug loading via incubation to preserve the functional integrity of the membrane. However, this may contribute to the low drug loading efficiency, that a more efficient method for loading MTX should be further explored. Assessing drug release from exosomes and drug accumulation within cells provides valuable information about drug delivery kinetics and the potential for sustained drug release [55]. Anti-CD19-Exo-MTX exhibited enhanced accessibility to lymphoma cells and sustained intracellular accumulation over an extended duration, compared to free drugs. In our vivo imaging results showed that fluorescence signals of Vivo Track DiR-labeled exosomes at the tumor site were observed with anti-CD19-Exo-MTX, demonstrating the ability to accumulate in tumor tissue, while Exo-MTX exhibited systemic distribution. The distribution of MTX from anti-CD19-Exo exhibited a time-dependent pattern, and the peak fluorescence intensity occurred at 24 h. Anti-CD19-Exo significantly increased MTX distribution in CSF compared with Exo, potentially due to the CD19 modification targeting these exosomes to tumor sites, which may lead to their prolonged retention in the CSF. This targeted delivery is hypothesized to reduce the clearance rate of these vesicles relative to unmodified Exo, thereby substantially increasing the MTX concentration within the CSF.

Research has indicated that all exosomes could cross the BBB with different traversal rates [56]. However, the mechanistic pathways by which exosomes cross the BBB have not been fully elucidated yet [57]. There are multiple pathways for molecules and cells to cross the BBB, including paracellular diffusion, transcellular diffusion, carrier-mediated transport, receptor-mediated transport, adsorptive-mediated transport and cell-mediated transport [30, 58]. Various methods of cell-exosome interaction have been proposed, with receptor-mediated endocytosis being a widely used mechanism by various cells [59]. Our study showed that anti-CD19-Exo-MTX crossed the BBB via receptor-mediated endocytosis, consistent with the literature. After endocytosis, exosomes are either degraded by lysosomes or incorporated into endosomes, where they form multivesicular body (MVB) and are subsequently transported to the plasma membrane as newly formed intraluminal vesicles (ILV) within the recipient cell [60]. Further investigation is needed to explore the various mechanisms by which exosomes cross the BBB, considering their cellular origin and differing environmental factors.

Safety and toxicity should also be given attention. Researches have shown that iRGD-modified exosomes derived from brain endothelial cells and anti-CD22-modified exosomes derived from 293T cells, loaded with DOX, can be used for targeted therapy in PCNSL models [47, 61]. The increase in targeted modification allows the drug to accumulate in tumor tissues, thereby reducing side effects in non-targeted tissues. Treatment with anti-CD19-Exo-MTX showed no significant histological damage to vital organs, indicating good safety and no toxicity or side effects in animals. Particularly, we were pleasantly surprised to find that the exosome-mediated delivery of MTX showed signs of neuroprotection, liver regeneration and alleviation of kidney inflammation. Therefore, we conducted a proteomic analysis of exosomes derived from hAMSCs and indeed found that exosomes from

hAMSCs are involved in pathways such as neuroprotection, hepatic protection, and renal protection. After administration, we conducted additional TUNEL staining and Nissl staining on the brain tissues of mice, revealing that hAMSCs-derived exosomes effectively alleviate the neurotoxicity induced by MTX. Meanwhile, compared to the MTX group, the exosome groups showed no significant increase in AST, ALT, CREA, or IL-6 levels, nor a reduction in blood cell counts. In addition, we further confirmed the protective effects of exosomes on HT22 and HK-2 cells at the cellular level. However, potential long-term effects and the specific molecular mechanisms by which exosomes derived from hAMSCs alleviate MTX-induced neurotoxicity, hepatotoxicity, and nephrotoxicity require further investigation.

Despite the promising results of anti-CD19-Exo-MTX in both cellular and animal models, several challenges remain that must be addressed before its clinical application. A major concern is the negative charge on the surface of exosomes, which may cause electrostatic repulsion with the negatively charged brain endothelial cells, potentially hindering their endocytosis [62]. To enhance exosome-mediated drug delivery across the BBB, modifying the surface charge of exosomes could be a promising strategy[63]. Moreover, the current limitations in exosome isolation and detection techniques present a significant challenge, affecting their scalability and consistency for clinical use. Future efforts should focus on developing more efficient and cost-effective methods for isolating exosomes while preserving their integrity. Additionally, further investigation into the variability of exosome contents is crucial, particularly in the context of their use as drug delivery vehicles.

Conclusion

In brief, we developed a novel drug delivery system anti-CD19-Exo-MTX that has a higher BBB permeability and target CNSL, achieved significant tumor growth inhibition and prolonged the survival time of CNSL models. In particular, it can reduce MTX-induced neurotoxicity, hepatotoxicity, and nephrotoxicity, demonstrating good biocompatibility and safety. We firmly believe that our research offers a reference for the further development of targeted delivery drugs for the treatment of CNSL.

Abbreviations

CNSL	Central nervous system lymphoma
BBB	Blood–brain barrier
MTX	Methotrexate
DDS	drug delivery systems
hAMSCs	Human adipose-derived mesenchymal stem cells
HPLC	High performance liquid chromatography
CSF	Cerebrospinal fluid
HD-MTX	High-dose methotrexate
MSCs	Mesenchymal stem cells
AMSCs	Adipose-derived mesenchymal stem cells
NHL	Non-Hodgkin lymphoma
MRI	Magnetic resonance imaging
LPL	Lipoprotein Lipase
ALP	Alkaline phosphatase
OCN	Osteocalcin
DLS	Dynamic light scattering
TEM	Transmission electron microscopy
TEER	Transendothelial electrical resistance
LC-MS/MS	Liquid chromatograph - tandem mass spectrometer
TUNEL	Terminal deoxynucleotidyl transferase biotin-dUTP nick end labeling
AST	Aspartate aminotransferase
ALT	Alanine aminotransferase
CREA	Creatinine
WBC	White blood cells
NE	Neutrophils
RBC	Red blood cells
HB	Hemoglobin
PLT	Platelet
MVB	Multivesicular body
ILV	Intraluminal vesicles

Supplementary Information

The online version contains supplementary material available at https://doi.org/10.1186/s12951-025-03238-9.

Additional file 1.

Additional file 2.

Additional file 3.

Additional file 4.

Additional file 5.

Acknowledgements

This work was supported by the National Natural Science Foundation of China (82270197, 82270211, 82470199); the Priority Academic Program Development of Jiangsu Higher Education Institutions; Suzhou City Basic Research Program - Key Clinical Technology Research (SKY2023010); The Project of State Key Laboratory of Radiation Medicine and Protection, Soochow University (GZK12023020); The special project of "Technological innovation" project of CNNC Medical Industry Co. Ltd (ZHYLYB2021002); Suzhou Science and Technology Agency Project (SKYD2023215).

Author contributions

B.Z.L and W.Z.Z. designed the research, and contributed reagents and other essential materials. M.F.Z. performed research and wrote the paper. Q.L., Y.L.C., R.R., L.X.H., Y.C.Z., H.X.C., H.X., X.Y.Z. and Z.M.W. analyzed data. S.S.Y., M.L.C., C.H., H.Z., L.L.Q., R.J.H. and X.Y.Z. modified the paper. All authors reviewed the manuscript.

Funding

National Natural Science Foundation of China (82270197, 82270211, 82470199); the Priority Academic Program Development of Jiangsu Higher Education Institutions; Suzhou City Basic Research Program - Key Clinical Technology Research (SKY2023010); The Project of State Key Laboratory of Radiation Medicine and Protection, Soochow University (GZK12023020); The special project of "Technological innovation" project of CNNC Medical Industry Co. Ltd (ZHYLYB2021002); Suzhou Science and Technology Agency Project (SKYD2023215).

Availability of data and materials

No datasets were generated or analysed during the current study.

Declarations

Ethics approval and consent to participate
The animal experimentation acquired permission from the ethics committee of Soochow University. All human adipose tissue samples were collected from the Second Affiliated Hospital of Soochow University after receiving permission from the ethics committee of the Second Affiliated Hospital of Soochow University. Informed written consent was obtained from each subject or each subject's guardian. The study was conducted in accordance with the Declaration of Helsinki.

Consent for publication
Not applicable.

Competing interests
The authors declare no competing interests.

Author details
[1]Department of Hematology, The Second Affiliated Hospital of Soochow University, San Xiang Road 1055, Suzhou 215006, China. [2]Department of Cell Biology, School of Basic Medical Sciences, Soochow University, Ren Ai Road 199, Suzhou 215123, China. [3]Xi'an Jiaotong-Liverpool University, Suzhou, China. [4]Suzhou Sano Precision Medicine Ltd., Suzhou, China.

Received: 20 December 2024 Accepted: 17 February 2025
Published online: 05 March 2025

References

1. Schaff LR, Grommes C. Primary central nervous system lymphoma. Blood. 2022;140(9):971–9.
2. Pardridge WM. Drug transport across the blood-brain barrier. J Cereb Blood Flow Metab. 2012;32(11):1959–72.
3. Rana S, Dranchak P, Dahlin JL, Lamy L, Li W, Oliphant E, et al. Methotrexate-based PROTACs as DHFR-specific chemical probes. Cell Chem Biol. 2024;31(2):221-233e14.
4. Fahey JB, DiMaggio C. High-dose methotrexate and primary central nervous system lymphoma. J Neurosci Nurs. 2007;39(2):83–8.
5. Ferreira D, Moreira JN, Rodrigues LR. New advances in exosome-based targeted drug delivery systems. Crit Rev Oncol Hematol. 2022;172: 103628.
6. Deshmukh V, Pathan NS, Haldar N, Nalawade S, Narwade M, Gajbhiye KR, et al. Exploring intranasal drug delivery via nanocarriers: A promising glioblastoma therapy. Colloids Surf B Biointerfaces. 2025;245: 114285.
7. Amarandi RM, Ibanescu A, Carasevici E, Marin L, Dragoi B. Liposomal-based formulations: A path from basic research to temozolomide delivery inside glioblastoma tissue. Pharmaceutics. 2022;14(2):308.
8. Tian T, Zhang HX, He CP, Fan S, Zhu YL, Qi C, et al. Surface functionalized exosomes as targeted drug delivery vehicles for cerebral ischemia therapy. Biomaterials. 2018;150:137–49.
9. Kamerkar S, LeBleu VS, Sugimoto H, Yang S, Ruivo CF, Melo SA, et al. Exosomes facilitate therapeutic targeting of oncogenic KRAS in pancreatic cancer. Nature. 2017;546(7659):498–503.
10. Colombo M, Raposo G, Thery C. Biogenesis, secretion, and intercellular interactions of exosomes and other extracellular vesicles. Annu Rev Cell Dev Biol. 2014;30:255–89.
11. Zhang X, Zhang H, Gu J, Zhang J, Shi H, Qian H, et al. Engineered extracellular vesicles for cancer therapy. Adv Mater. 2021;33(14): e2005709.
12. Thery C, Ostrowski M, Segura E. Membrane vesicles as conveyors of immune responses. Nat Rev Immunol. 2009;9(8):581–93.
13. Hornung V, Bauernfeind F, Halle A, Samstad EO, Kono H, Rock KL, et al. Silica crystals and aluminum salts activate the NALP3 inflammasome through phagosomal destabilization. Nat Immunol. 2008;9(8):847–56.
14. Pidaparti M, Bostrom B. Comparison of allergic reactions to pegasparaginase given intravenously versus intramuscularly. Pediatr Blood Cancer. 2012;59(3):436–9.
15. Aryani A, Denecke B. Exosomes as a nanodelivery system: A key to the future of neuromedicine? Mol Neurobiol. 2016;53(2):818–34.
16. Manterola L, Guruceaga E, Gallego Perez-Larraya J, Gonzalez-Huarriz M, Jauregui P, Tejada S, et al. A small noncoding RNA signature found in exosomes of GBM patient serum as a diagnostic tool. Neuro Oncol. 2014;16(4):520–7.
17. Mei R, Qin W, Zheng Y, Wan Z, Liu L. Role of adipose tissue derived exosomes in metabolic disease. Front Endocrinol (Lausanne). 2022;13: 873865.
18. Bonomi A, Cocce V, Cavicchini L, Sisto F, Dossena M, Balzarini P, et al. Adipose tissue-derived stromal cells primed in vitro with paclitaxel acquire anti-tumor activity. Int J Immunopathol Pharmacol. 2013;26(1 Suppl):33–41.
19. Chen H, Wang L, Zeng X, Schwarz H, Nanda HS, Peng X, et al. Exosomes, a new star for targeted delivery. Front Cell Dev Biol. 2021;9: 751079.
20. Mosquera-Heredia MI, Morales LC, Vidal OM, Barcelo E, Silvera-Redondo C, Velez JI, et al. Exosomes: Potential disease biomarkers and new therapeutic targets. Biomedicines. 2021;9(8):1061.
21. Kooijmans SAA, Schiffelers RM, Zarovni N, Vago R. Modulation of tissue tropism and biological activity of exosomes and other extracellular vesicles: New nanotools for cancer treatment. Pharmacol Res. 2016;111:487–500.
22. Armstrong JP, Holme MN, Stevens MM. Re-engineering extracellular vesicles as smart nanoscale therapeutics. ACS Nano. 2017;11(1):69–83.
23. Alvarez-Erviti L, Seow Y, Yin H, Betts C, Lakhal S, Wood MJ. Delivery of siRNA to the mouse brain by systemic injection of targeted exosomes. Nat Biotechnol. 2011;29(4):341–5.
24. Lou G, Song X, Yang F, Wu S, Wang J, Chen Z, et al. Exosomes derived from miR-122-modified adipose tissue-derived MSCs increase chemosensitivity of hepatocellular carcinoma. J Hematol Oncol. 2015;8:122.
25. Ohno S, Takanashi M, Sudo K, Ueda S, Ishikawa A, Matsuyama N, et al. Systemically injected exosomes targeted to EGFR deliver antitumor microRNA to breast cancer cells. Mol Ther. 2013;21(1):185–91.
26. Siddiqi T, Wang X, Blanchard MS, Wagner JR, Popplewell LL, Budde LE, et al. CD19-directed CAR T-cell therapy for treatment of primary CNS lymphoma. Blood Adv. 2021;5(20):4059–63.
27. Li Y, Zhu J, Yang Y, Chen Y, Liu L, Tao J, et al. Long-acting nanohybrid hydrogel induces persistent immunogenic chemotherapy for suppressing postoperative tumor recurrence and metastasis. Mol Pharm. 2023;20(12):6345–57.
28. Park JS, Choe K, Khan A, Jo MH, Park HY, Kang MH, et al. Establishing co-culture blood-brain barrier models for different neurodegeneration conditions to understand its effect on BBB integrity. Int J Mol Sci. 2023;24(6):5283.
29. Nishihara H, Perriot S, Gastfriend BD, Steinfort M, Cibien C, Soldati S, et al. Intrinsic blood-brain barrier dysfunction contributes to multiple sclerosis pathogenesis. Brain. 2022;145(12):4334–48.
30. Deli MA, Abraham CS, Kataoka Y, Niwa M. Permeability studies on in vitro blood-brain barrier models: physiology, pathology, and pharmacology. Cell Mol Neurobiol. 2005;25(1):59–127.
31. Chatard M, Puech C, Roche F, Perek N. Hypoxic stress induced by hydralazine leads to a loss of blood-brain barrier integrity and an increase in efflux transporter activity. PLoS One. 2016;11(6): e0158010.
32. Sawaftah NA, Paul V, Awad N, Husseini GA. Modeling of anti-cancer drug release kinetics from liposomes and micelles: a review. IEEE Trans Nanobiosci. 2021;20(4):565–76.
33. Hashimoto M, Nasser H, Chihara T, Suzu S. Macropinocytosis and TAK1 mediate anti-inflammatory to pro-inflammatory macrophage differentiation by HIV-1 Nef. Cell Death Dis. 2014;5(5): e1267.
34. Saeed MF, Kolokoltsov AA, Albrecht T, Davey RA. Cellular entry of ebola virus involves uptake by a macropinocytosis-like mechanism and subsequent trafficking through early and late endosomes. PLoS Pathog. 2010;6(9): e1001110.
35. Macia E, Ehrlich M, Massol R, Boucrot E, Brunner C, Kirchhausen T. Dynasore, a cell-permeable inhibitor of dynamin. Dev Cell. 2006;10(6):839–50.
36. Chen YC, Sheen JM, Wang SC, Hsu MH, Hsiao CC, Chang KA, et al. Methotrexate neurotoxicity is related to epigenetic modification of the myelination process. Int J Mol Sci. 2021;22(13):6718.
37. Familtseva A, Jeremic N, Tyagi SC. Exosomes: cell-created drug delivery systems. Mol Cell Biochem. 2019;459(1–2):1–6.
38. Kalluri R, LeBleu VS. The biology, function, and biomedical applications of exosomes. Science. 2020;367(6478): eaau6977.

39. Abdelgawad M, Bakry NS, Farghali AA, Abdel-Latif A, Lotfy A. Mesenchymal stem cell-based therapy and exosomes in COVID-19: current trends and prospects. Stem Cell Res Ther. 2021;12(1):469.
40. Wang R, Ma WG, Gao GD, Mao QX, Zheng J, Sun LZ, et al. Fluoro jade-C staining in the assessment of brain injury after deep hypothermia circulatory arrest. Brain Res. 2011;1372:127–32.
41. Smith FM, Raghupathi R, MacKinnon MA, McIntosh TK, Saatman KE, Meaney DF, et al. TUNEL-positive staining of surface contusions after fatal head injury in man. Acta Neuropathol. 2000;100(5):537–45.
42. Schurr R, Mezer AA. The glial framework reveals white matter fiber architecture in human and primate brains. Science. 2021;374(6568):762–7.
43. Doolittle ND, Peereboom DM, Christoforidis GA, Hall WA, Palmieri D, Brock PR, et al. Delivery of chemotherapy and antibodies across the blood-brain barrier and the role of chemoprotection, in primary and metastatic brain tumors: report of the Eleventh Annual Blood-Brain Barrier Consortium meeting. J Neurooncol. 2007;81(1):81–91.
44. Lu G, Wang X, Li F, Wang S, Zhao J, Wang J, et al. Engineered biomimetic nanoparticles achieve targeted delivery and efficient metabolism-based synergistic therapy against glioblastoma. Nat Commun. 2022;13(1):4214.
45. Liu Y, Li D, Liu Z, Zhou Y, Chu D, Li X, et al. Targeted exosome-mediated delivery of opioid receptor Mu siRNA for the treatment of morphine relapse. Sci Rep. 2015;5:17543.
46. Sadeghi S, Tehrani FR, Tahmasebi S, Shafiee A, Hashemi SM. Exosome engineering in cell therapy and drug delivery. Inflammopharmacology. 2023;31(1):145–69.
47. Liu X, Xia T, Fang Y, Zuo H, Dong X, Xu P, et al. Overcoming the blood-brain barrier by using a multistage exosome delivery system to inhibit central nervous system lymphoma. Nanomedicine. 2022;41: 102523.
48. Wang C, Li N, Li Y, Hou S, Zhang W, Meng Z, et al. Engineering a HEK-293T exosome-based delivery platform for efficient tumor-targeting chemotherapy/internal irradiation combination therapy. J Nanobiotechnol. 2022;20(1):247.
49. Rao D, Huang D, Sang C, Zhong T, Zhang Z, Tang Z. Advances in mesenchymal stem cell-derived exosomes as drug delivery vehicles. Front Bioeng Biotechnol. 2021;9: 797359.
50. Hajinejad M, Sahab-Negah S. Neuroinflammation: The next target of exosomal microRNAs derived from mesenchymal stem cells in the context of neurological disorders. J Cell Physiol. 2021;236(12):8070–81.
51. Nakano M, Fujimiya M. Potential effects of mesenchymal stem cell derived extracellular vesicles and exosomal miRNAs in neurological disorders. Neural Regen Res. 2021;16(12):2359–66.
52. Liu H, Nie T, Duan X, Zhang X, Zheng Y, Zhong W, et al. Cerebral delivery of redox-responsive lenalidomide prodrug plus methotrexate for primary central nerve system lymphoma combination therapy. J Control Release. 2023;359:132–46.
53. Neelapu SS, Chavez JC, Sehgal AR, Epperla N, Ulrickson M, Bachy E, et al. Three-year follow-up analysis of axicabtagene ciloleucel in relapsed/refractory indolent non-Hodgkin lymphoma (ZUMA-5). Blood. 2024;143(6):496–506.
54. Locke FL, Filosto S, Chou J, Vardhanabhuti S, Perbost R, Dreger P, et al. Impact of tumor microenvironment on efficacy of anti-CD19 CAR T cell therapy or chemotherapy and transplant in large B cell lymphoma. Nat Med. 2024;30(2):507–18.
55. Chen Z, Xiong M, Tian J, Song D, Duan S, Zhang L. Encapsulation and assessment of therapeutic cargo in engineered exosomes: a systematic review. J Nanobiotechnol. 2024;22(1):18.
56. Banks WA, Sharma P, Bullock KM, Hansen KM, Ludwig N, Whiteside TL. Transport of extracellular vesicles across the blood-brain barrier: brain pharmacokinetics and effects of inflammation. Int J Mol Sci. 2020;21(12):4407.
57. Abdelsalam M, Ahmed M, Osaid Z, Hamoudi R, Harati R. Insights into exosome transport through the blood-brain barrier and the potential therapeutical applications in brain diseases. Pharmaceuticals (Basel). 2023;16(4):571.
58. Sanchez-Dengra B, Gonzalez-Alvarez I, Sousa F, Bermejo M, Gonzalez-Alvarez M, Sarmento B. In vitro model for predicting the access and distribution of drugs in the brain using hCMEC/D3 cells. Eur J Pharm Biopharm. 2021;163:120–6.
59. Gonda A, Kabagwira J, Senthil GN, Wall NR. Internalization of exosomes through receptor-mediated endocytosis. Mol Cancer Res. 2019;17(2):337–47.
60. Tian T, Zhu YL, Hu FH, Wang YY, Huang NP, Xiao ZD. Dynamics of exosome internalization and trafficking. J Cell Physiol. 2013;228(7):1487–95.
61. Xia T, Liu Z, Du Y, Zhang J, Liu X, Ouyang J, et al. Bifunctional iRGD-Exo-DOX crosses the blood-brain barrier to target central nervous system lymphoma. Biochem Pharmacol. 2024;223: 116138.
62. Duan X, Li Y. Physicochemical characteristics of nanoparticles affect circulation, biodistribution, cellular internalization, and trafficking. Small. 2013;9(9–10):1521–32.
63. Zhang C, Pathrikar TV, Baby HM, Li J, Zhang H, Selvadoss A, et al. Charge-reversed exosomes for targeted gene delivery to cartilage for osteoarthritis treatment. Small Methods. 2024;8(9): e2301443.

Publisher's Note